Article

Atomistic Study of the Role of Defects on $\alpha \rightarrow \epsilon$ Phase Transformations in Iron under Hydrostatic Compression

Hoang-Thien Luu [1], **Roberto G. A. Veiga** [2] **and Nina Gunkelmann** [1,*]

[1] Institute of Applied Mechanics, Clausthal University of Technology, Arnold-Sommerfeld-Straße, D-38678 Clausthal-Zellerfeld, Germany; hoang-thien.luu@tu-clausthal.de

[2] Center of Engineering, Modeling and Applied Social Sciences, Federal University of ABC, 09210-580 Santo André, Brazil; roberto.veiga@ufabc.edu.br

[*] Correspondence: nina.gunkelmann@tu-clausthal.de

Abstract: It has long been known that iron undergoes a phase transformation from body-centered cubic/α structure to the metastable hexagonal close-packed/ε phase under high pressure. However, the interplay of line and planar defects in the parent material with the transformation process is still not fully understood. We investigated the role of twins, dislocations, and Cottrell atmospheres in changing the crystalline iron structure during this phase transformation by using Monte Carlo methods and classical molecular dynamics simulations. Our results confirm that embryos of ε-Fe nucleate at twins under hydrostatic compression. The nucleation of the hcp phase is observed for single crystals containing an edge dislocation. We observe that the buckling of the dislocation can help to nucleate the dense phase. The crystal orientations between the initial structure α-Fe and ε-Fe in these simulations are $\{110\}_{bcc} \,||\, \{0001\}_{hcp}$. The presence of Cottrell atmospheres surrounding an edge dislocation in bcc iron retards the development of the hcp phase.

Keywords: solid–solid transitions; iron; carbon; molecular dynamics; cottrell atmosphere

1. Introduction

Understanding the behavior of iron under extreme conditions is important for geophysicists, astrophysicists and material scientists. For instance, shock-induced phase transformations provide insights into understanding meteoritic impacts and help to generate new materials with improved hardness properties, which are stable at ambient conditions. Pressure-induced phase transformations in iron were discovered in the mid-1950s by Bancroft [1]. Under a pressure of 13 GPa [2], body-centered cubic iron (bcc/α-Fe), which is stable at room conditions with atomic packing factor (APF) of 0.68 and coordination number of 8, transforms to hexagonal close-packed iron (hcp/ε-Fe) by a diffusionless transformation process. The hcp phase in iron has a coordination number of 12 and APF of 0.74, the same as face-centered cubic iron (fcc/γ-Fe), which is a product of the austenization process. It has been noted that α-Fe transforms to ε-Fe under static [3,4] or dynamic compression [5,6]. Diamond anvil cell measurements of iron up to 150 GPa have revealed the melting temperatures and densities at earth core conditions [7,8]. Shock waves show three distinct phases: The wave profiles feature first an elastic compression wave and then, after the elastic–plastic transition, the wave runs into the phase-transformed material. When the pressure is released, the dense phase transforms back to bcc iron exhibiting a decisive influence on the morphological properties of the material [4,9].

Density functional theory (DFT) results are very important to understand martensitic phase transformations under pressure in different materials [10–14]. The martensitic transformation in titanium has been analyzed and the DFT results are able to describe the experimental results [13–15]. DFT calculations [10–12] have confirmed the stability of hcp iron under high pressure and revealed the

transition barrier of the bcc/hcp phase transformation [12]. Using this approach, Friák [12,16] studied the bcc/hcp transition paths at the atomistic scale. However, since the transition is a kinetic process, the transformation does not simultaneously occur in the material.

Fisher [17] suggested that the martensite formation occurs randomly within a grain during the transformation. The parent grain is subdivided into smaller subgrains. Molecular dynamics (MD) simulations of single-crystal iron under hydrostatic compression [18] confirm the theory [17] that the hcp embryos are nucleated in the bulk such that many hcp cluster are formed during compression. Nonetheless, only a few studies have been carried out on the interplay between defects and hcp nucleation. By using highly accurate embedded-atom method (EAM) interatomic potentials [19,20] for the pressure-induced phase transformation in iron, MD simulations [5,18,20–22] using multimillion atoms revealed that dense clusters nucleate at grain boundaries and grow into the parent phase until they reach other dense clusters or grain boundaries. However, a detailed understanding of the nucleation of hcp iron at plane and line defects, in particular at dislocations, and the interplay with alloying elements, is still lacking. Although there exist experimental [23] and simulation studies [24] on the effect of pre-existing dislocations on martensitic phase transitions in iron, the impact on pressure induced phase transformations is still unclear. It is well known that clouds of carbon impurities will form in the surrounding of dislocations, the so-called Cottrell atmospheres [25,26]. These defects highly influence steel hardening as observed during strain aging. The interaction of carbon atoms with dislocations in bcc iron is the driving force leading to the formation of Cottrell atmospheres [25].

This study aimed at clarifying the effect of $1/2\langle 111\rangle$ $\{110\}$ edge dislocations, coherent twin boundaries and Cottrell atmospheres on the transition process, and the orientation relations between parent and daughter phases. The Ackland potential [20] has been used for a long time to study pressure-induced phase transformations. It is essential to understand the mobility of dislocations in the bulk. Depending on the slip planes, edge dislocations in iron obey different mobility laws. Dislocations move either by thermally activated nucleation or phonon drag dynamics for $1/2\langle 111\rangle$ $\{110\}$ dislocations or by single viscous drag for $1/2\langle 111\rangle$ $\{112\}$ dislocations [27]. Thus, the Frank–Read source model was used to investigate the behavior of dislocations under external load in this study. The results were compared with the prediction from discrete dislocation dynamics (DDD) simulations. The validity of the interatomic potential to reproduce the critical shear stress at the nanoscale was evaluated.

We present the simulation methods in Section 2 including the use of the interatomic embedded-atom method potential, the simulation setup for pressure-induced phase transformations, and the generation of Cottrell atmospheres. The different computational methods we used—molecular dynamics, Monte Carlo (MC), and DDD—are presented in Section 3. Detailed investigations of the evolution of the atomic systems provide insights into the mechanism of nucleation of hcp iron. Twins and dislocations play an important role in triggering the nucleation of the dense phase.

2. Materials and Methods

2.1. Interatomic Potentials

Molecular dynamics simulations are usually employed to study transformation pathways where the trajectory of atoms is predicted by numerically solving Newton's equation of motion. Interactions between atoms are defined by interatomic potentials. We used embedded-atom method (EAM) potentials, widely used for studying metallic materials [28].

The EAM Ackland potential [20] is particularly useful for studying pressure-induced phase transitions in iron [9,18,20,29–31]. Thus, the Ackland potential [20] is a good candidate for investigating the influence of defects to the diffusionless transformation process. Simulations for pure iron in this study used the Ackland potential, and we coupled the Ackland [20] and Hepburn [32] potential for studying the influence of the Cottrell atmosphere with 500 ppm of carbon (see Section 2.3).

2.2. MD Simulation Setup

The coherent twin boundary $\Sigma 3 (121) [\bar{1}01]$ is metastable in bcc iron. Tschopp et al. [33] analyzed various types of asymmetric/symmetric tilt, twist grain boundary structures by molecular static simulations and showed that low angle grain boundaries are an effective sink for vacancies and interstitial atoms along planes adjacent to grain boundary dislocations. To investigate the role of the $\Sigma 3$ boundary to the bcc/hcp phase transformation, we constructed crystals having a dimension of 29.6 mm $\times$ 20.3 mm $\times$ 11.6 nm, containing two and four coherent twin boundaries with roughly 600,000 atoms. The primary differences between the two models are the twin area and spacing between the boundaries. We investigated the contribution of the area of the defect to the bcc/hcp phase transformation to understand the occurrence of a large number of fcc atoms under shock compression which was reported by Kadau et al. [22].

The sample with two twin boundaries is shown in Figure 1. The crystal on the right is a mirror image of the left crystal with the mirror plane (121). The single-crystal containing four twin boundaries has a similar configuration, but the space between the two boundaries is half of the space compared to the model with two twin boundaries.
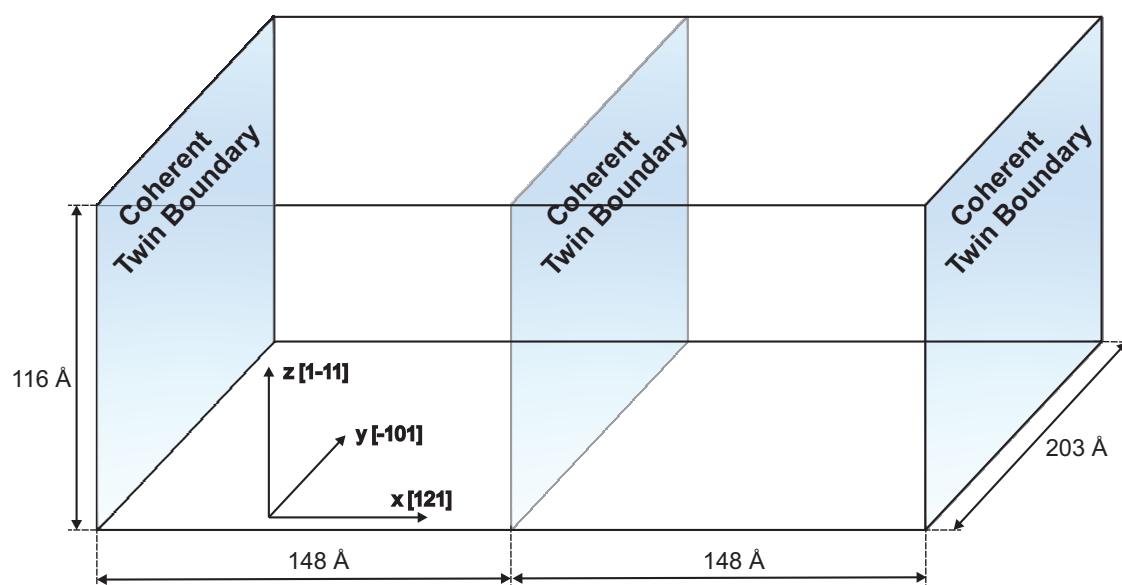

Figure 1. The simulation setup used to predict the behavior of crystals containing two coherent twin boundaries. Periodic boundary conditions were used for all three normal directions. The blue surface marks the (121) plane.

For the simulations on the effects of an edge dislocation, we constructed the simulation box shown in Figure 2, containing a single straight $1/2[111](\bar{1}01)$ edge dislocation, employing the open-source code Atomsk [34]. The sample size is the same as for the system containing twin boundaries. We adopted rigid boundary conditions (RBC) [35,36], terminated by free surfaces, in the $[\bar{1}01]$ direction, perpendicular to the glide plane. The iron atoms belonging to five atomic layers closest to the free surfaces were kept fixed to avoid spurious relaxations. Periodic boundary conditions were applied along the dislocation line, in [111] direction, and along the gliding direction, $[1\bar{2}1]$.
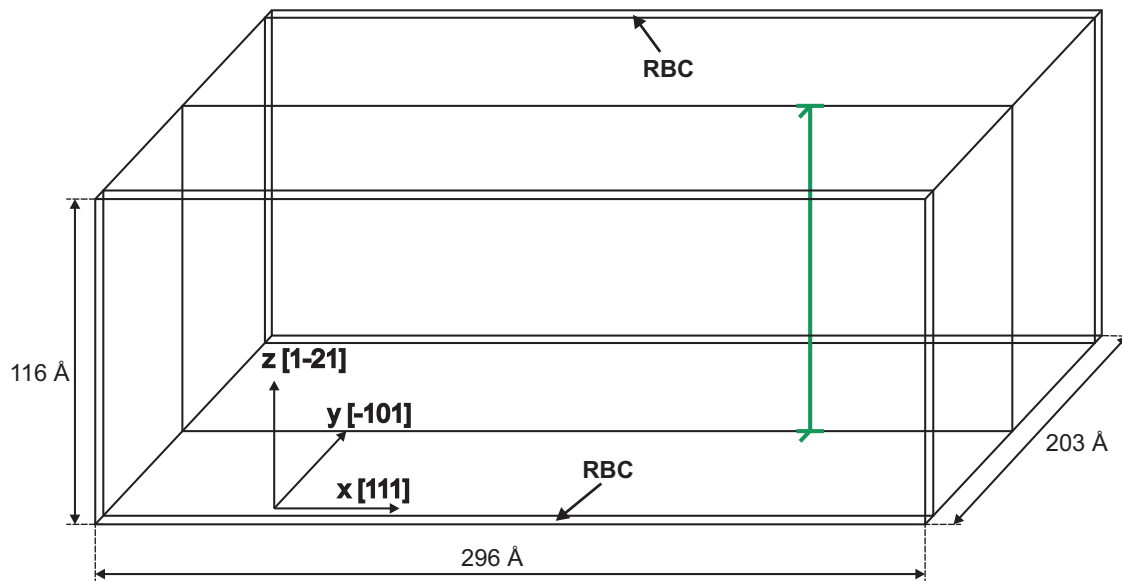
Figure 2. Simulation box containing a single $1/2[111](\bar{1}01)$ edge dislocation (green line). Periodic boundary conditions were used along $[1\bar{2}1]$ (x) and $[111]$ (z) directions, whereas rigid boundary conditions were applied along the $[\bar{1}01]$ (y) direction.

The simulations were carried out by the open-source molecular dynamics code LAMMPS [37]. Before hydrostatic compressions were applied at a temperature of 10 K, the systems used in our simulations were relaxed by an annealing procedure at a temperature of 800 K during 100 ps, below the austenitizing temperature of iron. The temperature was rescaled during heating from 10 K to 800 K and annealing from 800 K to 10 K within a period of 7 ps. The system normal pressure was kept at zero; it was independently controlled for each Cartesian direction. This relaxation technique has frequently been used to relax atomistic metallic structures [20,38]. The relaxed samples were subjected to hydrostatic compression at a strain rate of $1 \times 10^9 \text{ s}^{-1}$ in an NVE ensemble, and the maximum strain was 10%. Periodic boundary conditions were applied in all three normal directions for the crystal containing twins. The Verlet scheme with a time step of 0.5 fs was used in the simulations.

2.3. Monte Carlo Simulation Setup

The equilibrium C distribution around the single edge dislocation depicted in Figure 2 was estimated by on-lattice biased Monte Carlo in the NVT ensemble using the algorithm presented in Refs. [26,39]. Interstitial positions (octahedral sites) in this simulation box were mapped into a rigid lattice. Throughout the MC simulation, each site of the lattice had an occupancy of either 1 (occupied by a C atom) or 0 (unoccupied). To start the simulation, a number of sites, corresponding to 500 ppm of C, were selected at random and assigned an occupancy of 1. For the subsequent MC moves, which consisted of exchanging the occupancies of two sites, the energy of the resulting atomistic configuration was computed by LAMMPS after energy minimization. To speed up convergence, a bias was applied in which unoccupied sites near the dislocation line had a larger probability of being selected in the MC move. The difference between the total energies of the current configuration and the previous one was then used by the MC algorithm to accept or reject the move according to the well-known Metropolis MC scheme. In total, 100,000 MC iterations were performed before the equilibrium at 300 K was reached.

2.4. Atomic Structure Identification

The local crystal structure is one of the essential characteristics providing insights into the evolution of crystal defects, phase transition processes and the relationship between defects and material properties. Several methods can provide local structure characterization, such as Bond order

analysis [40], Common Neighbor Analysis [41], Centrosymmetry Parameter Analysis [42], Angular Distributions Analysis [43] and adaptive Common Neighbor Analysis (a-CNA) [44]. The a-CNA method is as a powerful method for systems containing complex local structures with more than two phases. In particular, volume changes during the phase transformation do not affect the accuracy of the detector due to an optimized cutoff radius for each atom. In this study, we employed the a-CNA algorithm implemented in OVITO [45] to identify the local crystal structure.

3. Results and Discussion

3.1. Frank–Read Source in bcc Iron

Material strength is characterized by the dynamics of dislocations; their movements allow plastic deformation in the bulk crystal. In face-centered cubic materials, an edge dislocation lying partly in an active glide plane and a pinning point at each end is a dislocation source or a Frank–Read source [46,47]. Under a shear stress higher than the critical stress, the dislocation is unstable leading to bowing-out of the dislocation and dislocation multiplication of loops. The generation of Frank–Read sources in MD simulations is highly nontrivial. Up to now, there are several MD models available in the literature [46–49], but they mainly focus on fcc materials. Very few studies [50] have examined Frank–Read sources in body-centered cubic crystals by using dislocation dynamics simulations. This section reports the behavior of dislocations generated by a Frank–Read source under shear stress and compares the results to dislocation dynamics simulations to verify the interatomic potential.

We adopt the model proposed by Shimokawa et al. [47] revealing realistic dislocation emission and bowing-out behavior of $\frac{1}{2}$ [111] (01$\bar{1}$), and $\frac{1}{2}$ [111] ($\bar{1}$2$\bar{1}$) edge dislocations. A sketch of the model is shown in Figure 3. The dimensions of the system in Burgers vector and edge dislocation direction are 25 nm; the length in normal direction to the dislocation is 2 nm. Two cylindrical holes of radius 0.5 nm in the direction normal to the glide plane are placed at both ends of the dislocation acting as pinning points. The distance between the two holes is larger than 8 nm. The Frank–Read system was relaxed under zero pressure boundary condition for 10 ps at a temperature of 300 K followed by temperature rescaling to 10 K in 2 ps. Then, the system was subjected to shear deformation with a strain rate of 5×10^8 s^{-1}.
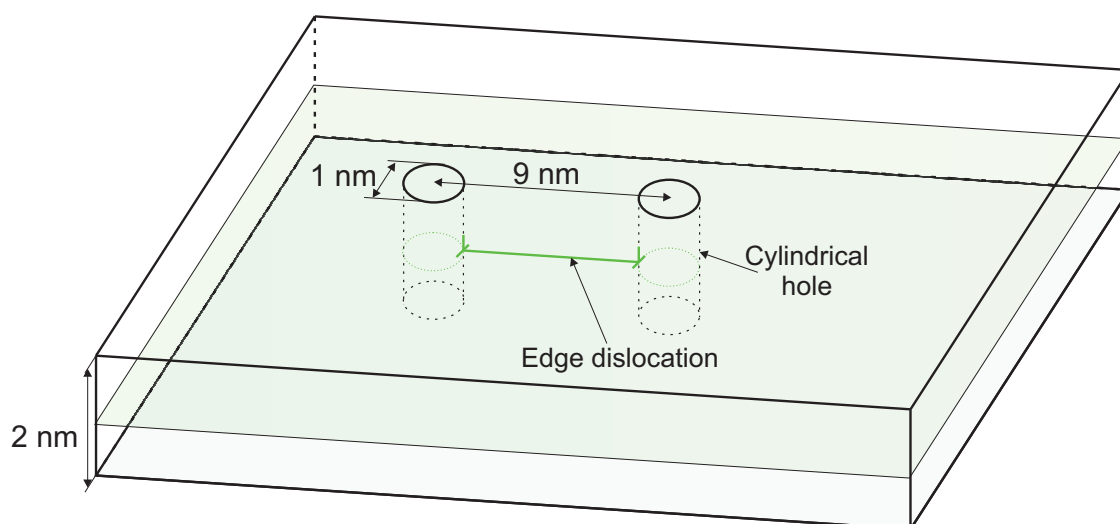

Figure 3. Model of the Frank–Read source in iron showing a dislocation segment of length 9 nm terminated by cylindrical holes of radius 0.5 nm.

For the $\frac{1}{2}$ [111] (01$\bar{1}$) dislocation, for small strains, the mobility of the dislocation is rather small. Later, the dislocation velocity increases linearly with strain, an evidence of viscous dynamics effects. At a shear strain of 6.5%, corresponding to a shear stress of 0.38 GPa, the dislocation reaches its stable

state and the dislocation segment responds to the force by bowing-out. In contrast, for the $\frac{1}{2}$ [111] $(\bar{1}2\bar{1})$ dislocation, we observed the nucleation of a kink-pair at a shear strain of 3% and a shear stress of 0.21 GPa. At higher strains, the bow-out of the dislocation is observed at a shear strain and stress of 8.5% and 0.55 GPa, respectively. The dynamic regimes of both dislocations are consistent with MD results from Queyreau et al. [27]. The dislocation bow-out shear stresses are in agreement with the critical values obtained by MD simulations from Shimokawa et al. [47]. Note that the critical shear stress for dislocation bow-out increases with decreasing length of the dislocation.

To verify the result of our MD simulations, we performed discrete dislocation dynamics simulations. For the DDD simulations, the following material properties of iron are used: shear modulus $\mu = 86$ GPa, Poisson ratio $\nu = 0.291$, Burgers vector $b = 0.2482$ nm and drag coefficient $\eta = 1 \times 10^{-4}$ Pas. Note that dislocation motion in body-centered cubic metals is of special complexity resulting in a strong temperature dependence of the flow stress, and in shear deformation asymmetries relative to the loading direction as well as crystal orientation [51]. We used the DDD framework by Po et al. [52] where a phenomenological dislocation mobility law for bcc metals is implemented [51]. The Frank–Read source has a length of 100 b and moves on the slip system [111]$(1\bar{1}0)$. We applied a shear stress of 0.01 GPa. For this low shear stress, the dislocation mobility was thermally activated. Figure 4 shows the evolution of the dislocation structure. We observed that the shape of the dislocation is hemispherical and screw arms do not generate. This is in agreement with the results by Fitzgerald et al. [50] for this slip system, who stated that a large energy difference exists between edge and screw, and the corners which appear do not allow the source to circumvent the screw-edge asymmetry. Note that in the MD simulations we simulated at constant strain rate and in DDD at constant small shear stress. At larger shear stress for DDD, screw arms are generated. Here, MD and DDD simulations are in agreement. Note that MD at high strain rates can lead to high stresses, as noted by Domain et al. [53].
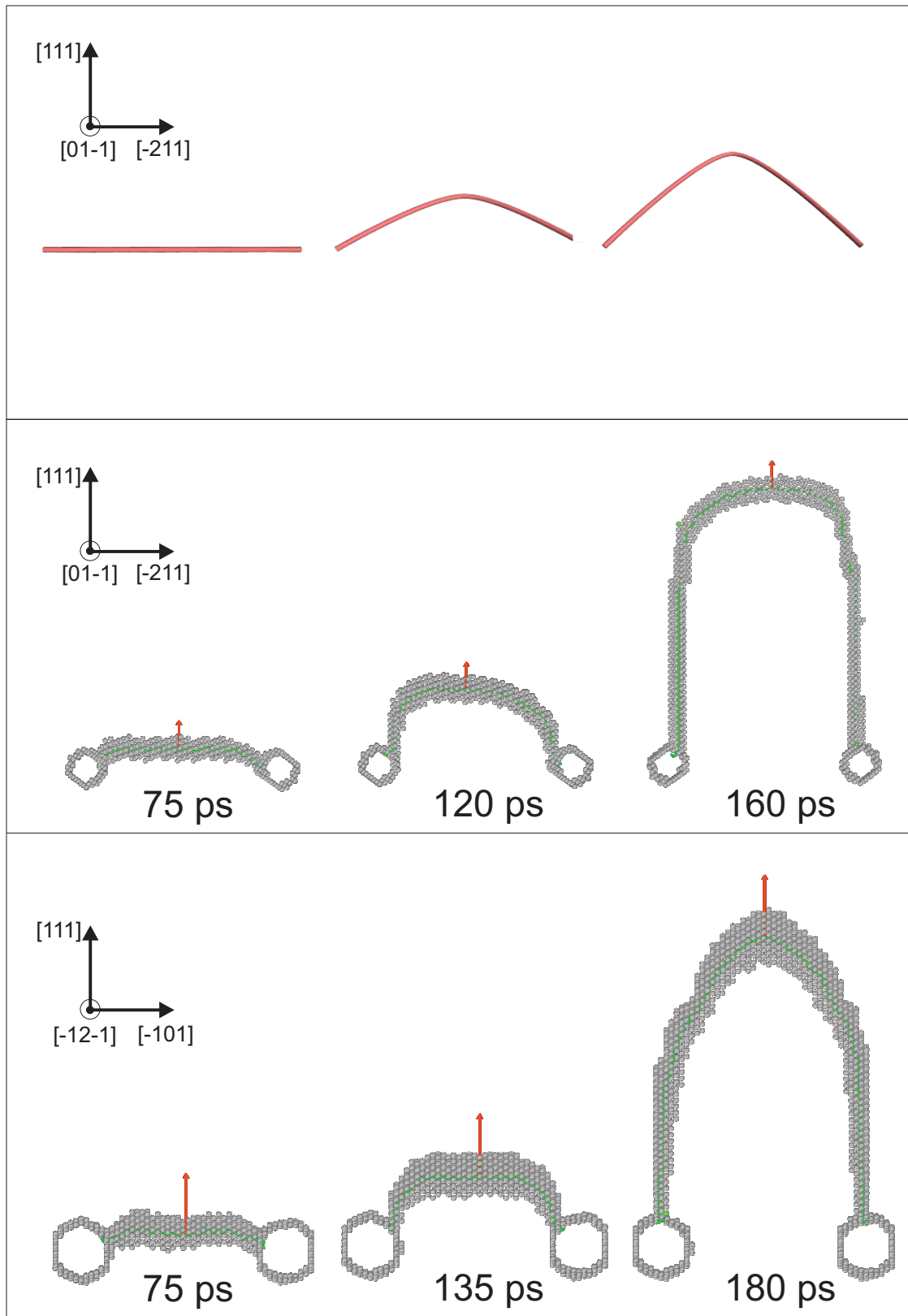
Figure 4. Dislocation mobility of an edge dislocation under shear deformation from the Frank–Read source in iron. Top: DDD simulation; Middle and bottom: MD simulations under shear deformation with a strain rate of 5×10^8 s^{-1} for two different slip systems. The dislocation is detected by the Dislocation analysis algorithm implemented in OVITO [45]. It is surrounded by disordered atoms in grey.

3.2. Pressure-Induced Phase Transformation

The symmetric tilt $\Sigma 3\,(121)\,[\bar{1}01]$ boundary in bcc is shown in Figure 5 (left). During rigid body translation under relaxation of a crystal containing a $\Sigma 3$ coherent twin boundary [54,55], one of the grains is slightly shifted in $[1\bar{1}1]$ direction. After relaxation, we observe at the coherent twin boundaries a slightly shifted and broken mirror plane as described in the literature [54,55] (see Figure 5, right). On the $(\bar{1}01)$ plane, the bcc structure atoms on one side are reflected at the twin boundaries (atoms in grey) obeying a zigzag configuration.

The pressure-induced phase transformation is driven by the negative volume change of the sample [56]. Figure 6 shows the configurations of the systems at the beginning and at 30 ps (3.0% strain), where red arrows are the displacement vectors. We observe the nucleation of the hcp phase forming as clusters at twin boundaries at a hydrostatic strain of 2.5%.
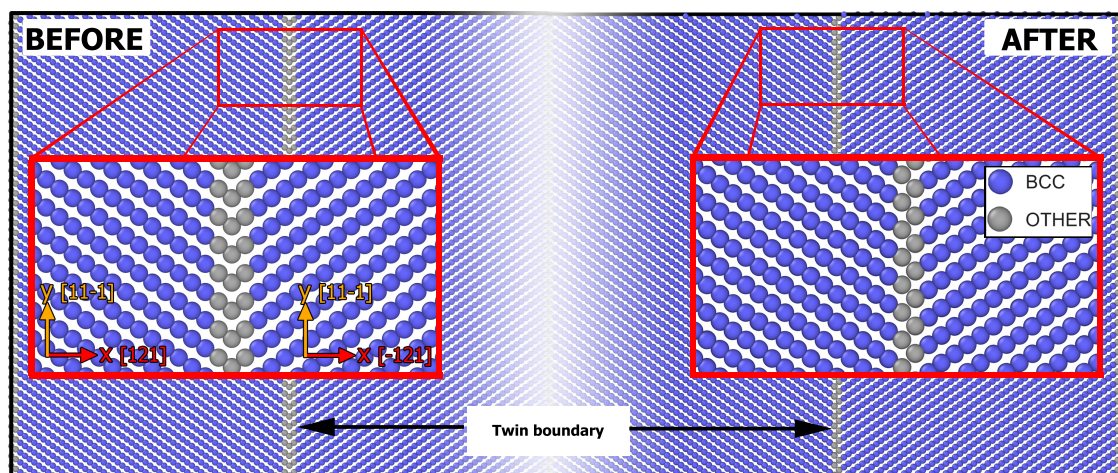

Figure 5. Visualization of the system configuration before and after relaxation on $(\bar{1}01)$ plane of a $\Sigma 3$ coherent twin boundary crystal. Atoms are colored according to crystal structure types (blue, bcc; grey, disordered atoms).
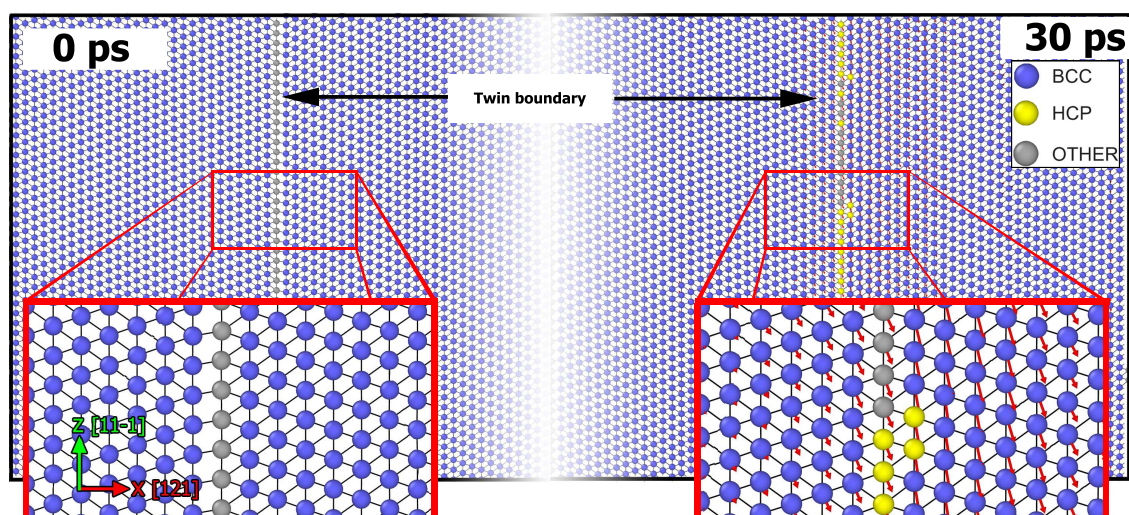

Figure 6. Snapshot of one layer of atoms on the $(\bar{1}01)$ plane of a single-crystal containing four coherent twin boundaries at 0 ps and 30 ps (3.0% strain). Atoms are colored according to crystal structure types (blue, bcc; yellow, hcp; grey, disordered atoms) and red arrows are displacement vectors. Connections between atoms are shown by black lines.

The volume fraction of hcp clusters increases during compression of the sample. At a strain of 4%, some hcp clusters having different orientations than the ones at the twin boundaries are

observed in the bulk crystal. In general, the orientation relation between parent and daughter phase is $\{110\}_{bcc} \,||\, \{0001\}_{hcp}$. This finding agrees with the proposed bcc/hcp transformation mechanism in Zirconium by Burgers [57] and in iron by Wang [58]. Once the transformation process is nearly complete, we observe the appearance of the fcc crystal structure. Some of the fcc clusters are formed as layers within the hcp phase. They are found to be stacking faults because the transformation path from $\{110\}_{bcc} \,||\, \{111\}_{fcc}$ is very close to the path from bcc to hcp. Some other fcc clusters are bounded by four hcp cluster with different directions. Figure 7 shows a snapshot of the $(\bar{1}01)$ plane at strain of 4% and 10% (after 40 ps and 100 ps), where atoms are colored by their local crystal structure.
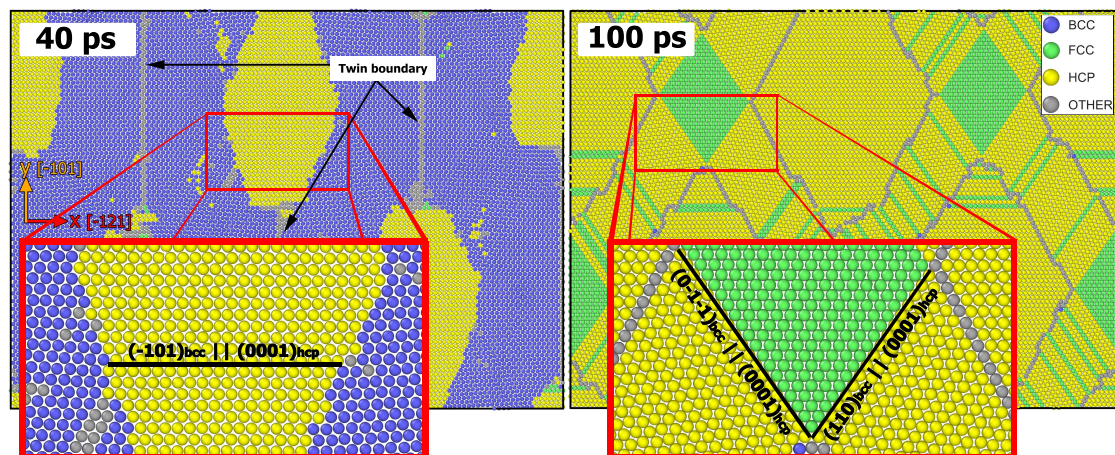

Figure 7. Snapshot of the $(\bar{1}01)$ plane of a single-crystal containing 4 coherent twin boundaries at a strain of 4% and 10% (40 ps and 100 ps) on the left and the right, respectively. Atoms are colored according to crystal structure types (blue, bcc; green, fcc; yellow, hcp; grey, disordered atoms).

The phase fraction versus strain, as shown in Figure 8, provides further information into the evolution of bcc, fcc, hcp, and defective structures during compression. The figure shows that a small fraction of hcp embryos is firstly formed at a strain of 2.5%, and followed by a rapid increase of hcp atoms after a strain of 3.5%. During the bcc/hcp phase transformation, the fcc phase fraction increases from 0.02 at a strain of 4.5% to 0.15 at 6% strain. Here, the volume fraction of this phase is 4.6 times smaller than the volume fraction of its counterpart hcp phase. The remaining bcc phase at a strain of 6% slowly transforms to hcp, while all other phase fractions remain steady at higher deformation. The sample with two coherent twin boundaries behaves similarly, but, in comparison to the previous case, the transformation process is slightly delayed. However, the transformation rate is approximately the same, and the phase fraction is almost tantamount at the end of the process.
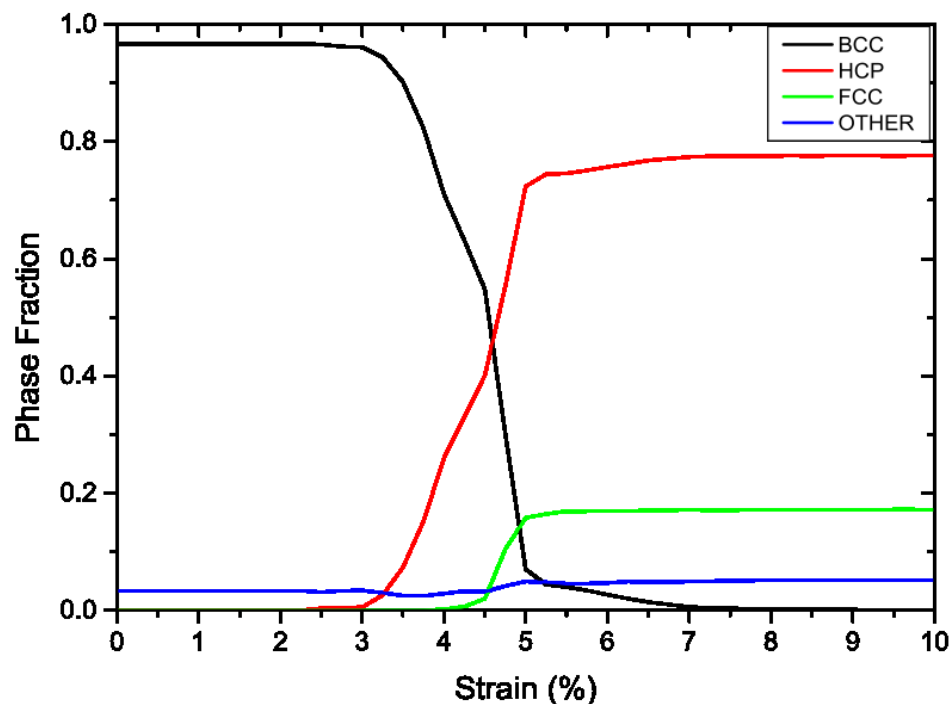
Figure 8. Phase fraction versus strain of a single-crystal containing four coherent twin boundaries under hydrostatic compression with a strain rate of 1×10^9 s^{-1}.

3.3. Edge Dislocation

Strong shock waves in metallic materials cause dislocation emissions and dislocation motions at the shock front [59]. Recent shock compression experiments [60] in Mg single-crystals show evidence of dislocation glide by using real-time X-ray diffraction. There are several models to predict the generation of dislocations at the shock front [59,61]. At such conditions, the deformation rate is normally large, but, in contrast, the self-recovery of the atomic structure surrounding defects is small. Therefore, dislocations tend to be reintegrated into stabilized defect structures [59].

The results obtained from the hydrostatic compression of an iron single-crystal containing a dislocation on $(\bar{1}01)$ with a Burgers vector $1/2\,[111]$ at a strain of 2.75% (27.5 ps) is shown in Figure 9. We observe buckling of the $1/2[111]\,(\bar{1}01)$ dislocation at high shear stress showing two kinks. The predicted behavior of the edge dislocation shown here is in agreement with experiments [59].
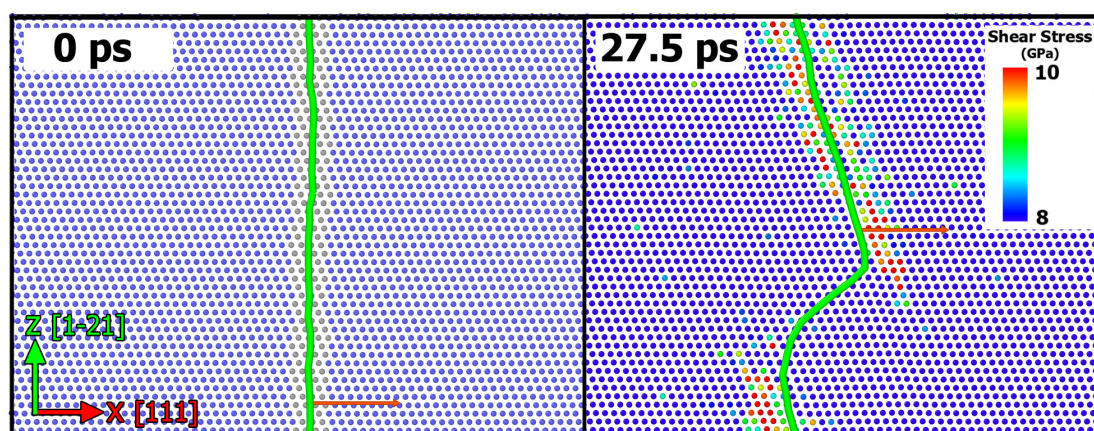

Figure 9. Dislocation shapes of the $1/2[111]\,(\bar{1}01)$ dislocation at 0 ps and 27.5 ps (2.5% strain). The original dislocation is on the left and the dislocation after compression at a strain of 2.75% (27.5 ps) is on the right. Atoms are colored according to their shear stress in GPa.

Note that an edge dislocation $1/2\langle 111\rangle$ on $\{110\}$ planes in body-centered cubic can be dissociated in two variants [62,63]:

$$\frac{1}{2}\,[\bar{1}11] = \frac{1}{8}\,[\bar{1}10] + \frac{1}{8}\,[\bar{3}34] \tag{1}$$

or

$$\frac{1}{2}\,[\bar{1}11] = \frac{1}{8}\,[\bar{1}10] + \frac{1}{4}\,[\bar{1}12] + \frac{1}{8}\,[\bar{1}10] \tag{2}$$

The second reaction is energetically favored [62]. Thus, the dislocation on $\{110\}$ planes may contribute to twinning in bcc materials [64]. An MD study [63] of bcc/hcp phase transformation in Zr single-crystals with an edge dislocation $1/2\langle 111\rangle\,\{\bar{1}01\}$ revealed that the kinetics of the diffusionless phase transformation is influenced by the dislocation. The phenomenon observed here is similar; the buckling of the dislocation and the nucleation of the hcp phase at 3% of strain are shown in Figure 10. We see that the nucleation of the hcp phase originates at the kinks of the dislocation where the curvature is largest. We also observed twin formation with habit planes parallel to $(110)_{bcc}$ before the propagation of hcp clusters proceeds. The orientation relation of parent and daughter phase is $(0\bar{1}1)_{bcc}\,||\,(0001)_{hcp}$. Here, the lattice distortion is highest resulting in an alleviated nucleation of the hcp phase.
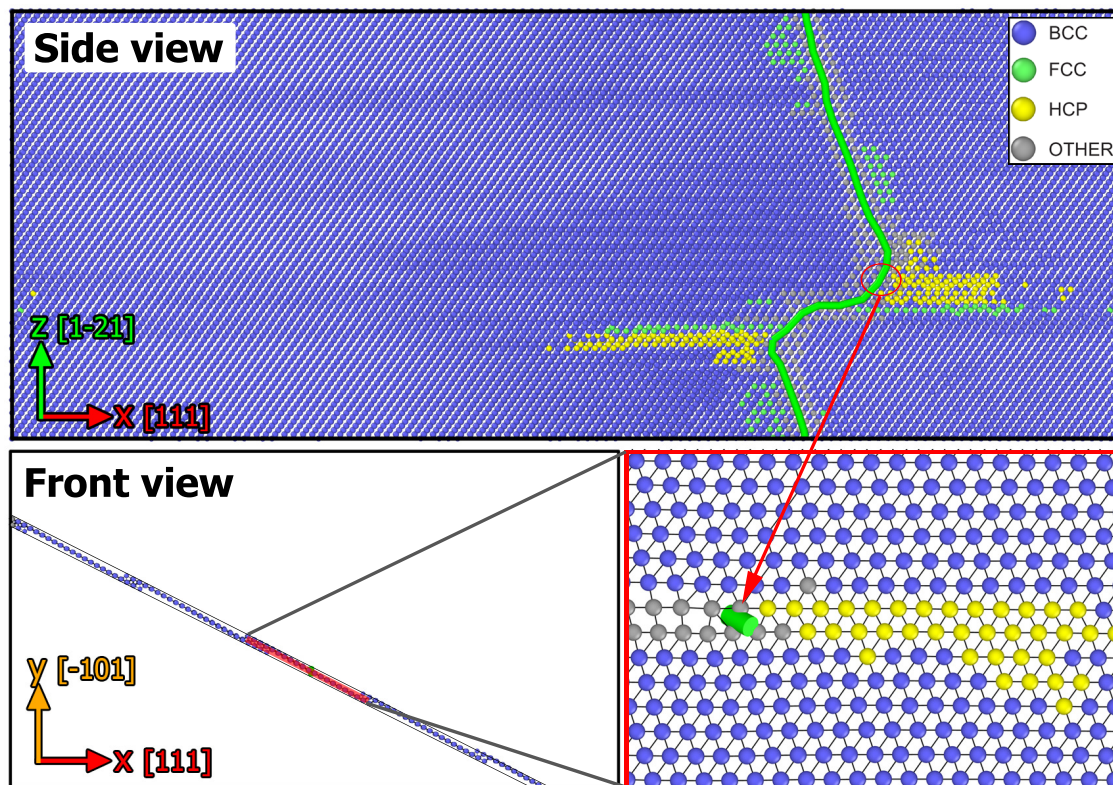

Figure 10. Snapshots showing side view, front view and a cross section of the dislocation (in green) and surrounding atoms at strain of 3% (30 ps). The side view shows the buckling of surrounding atoms and the nucleation of the hcp phase with a closer look of the nucleation of the hcp phase on the $(0\bar{1}1)$ plane. Atoms are colored according to crystal structure types (blue, bcc; green, fcc; yellow, hcp; grey, disordered atoms).

3.4. Cottrell Atmosphere

Carbon interactions with edge dislocations are known to be strong, with binding energies ranging from 0.66–0.78 eV per C atom, according to several elasticity calculations and atomistic simulations [65].

These interactions provide the driving force for the formation of carbon clouds decorating the line defect, the so-called Cottrell atmospheres. Indeed, after reaching equilibrium in the MC simulation, C segregation at the edge dislocation was clearly evidenced, as can be seen in Figure 11. One can see that C enrichment occurred mostly at the glide plane and in the planes below it, where the iron lattice is under tension. For the relatively low carbon concentration in this study (500 ppm), only a few interstitial atoms were found occupying octahedral sites in the compression part of the crystal. The maximum local C concentration, within one Burgers vector of the dislocation core, was observed to be as high as 10 at.%, also suggesting strong C segregation even for low total C concentrations. Although much above the solubility limit of C in bcc Fe, this high peak of local carbon concentration in the vicinity of a line defect was already reported in atom probe experiments [66].

For our simulation containing a Cottrell atmosphere, hcp phase clusters are observed inside the atmosphere at a strain of 3%. The presence of carbon destabilized the bcc lattice. However, the clusters cannot grow up as in the sample without carbon. A reason could be that carbon hinders the development of the dense phase [18]. In addition, the dislocation mobility is reduced by the Cottrell atmosphere. The transition is delayed until the hcp clusters in the bulk bcc material propagate and dominate the sample.
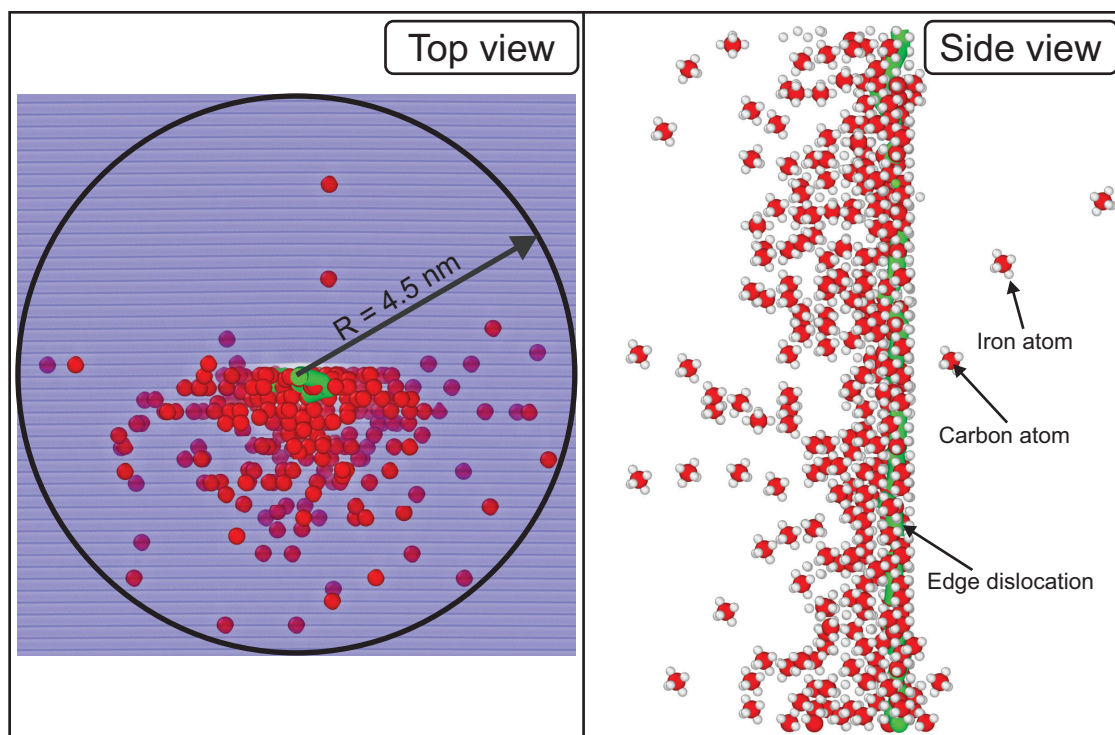

Figure 11. Snapshots showing the Carbon Cottrell atmosphere for the system equilibrated by MD simulations. (**Left**) Top view of the distribution of carbon atoms (red) in a radius of 4.5 nm from the edge dislocation, bcc iron is shown in blue. (**Right**) Side view where only carbon and disordered iron atoms (white) along the edge dislocation are shown.

The local atomic structures at the strain of 6% obtained from adaptive CNA are shown in Figure 12. Altogether, these snapshots provide important insights into the role of edge dislocations and Cottrell atmospheres to the pressure-induced transformation process in bcc iron. The $1/2[111]$ $(\bar{1}01)$ dislocation in bcc iron is associated with twinning. Twins parallel to $(110)_{bcc}$ result in a stacking fault that originates at planes parallel to the glide plane of the dislocation. One to three fcc layers interleave with the hcp phase. Therefore, a high fcc fraction is observed in this case. For the Cottrell atmosphere, the transformation does not start at planes parallel to the glide plane of the dislocation resulting in a higher hcp and smaller fcc fraction.
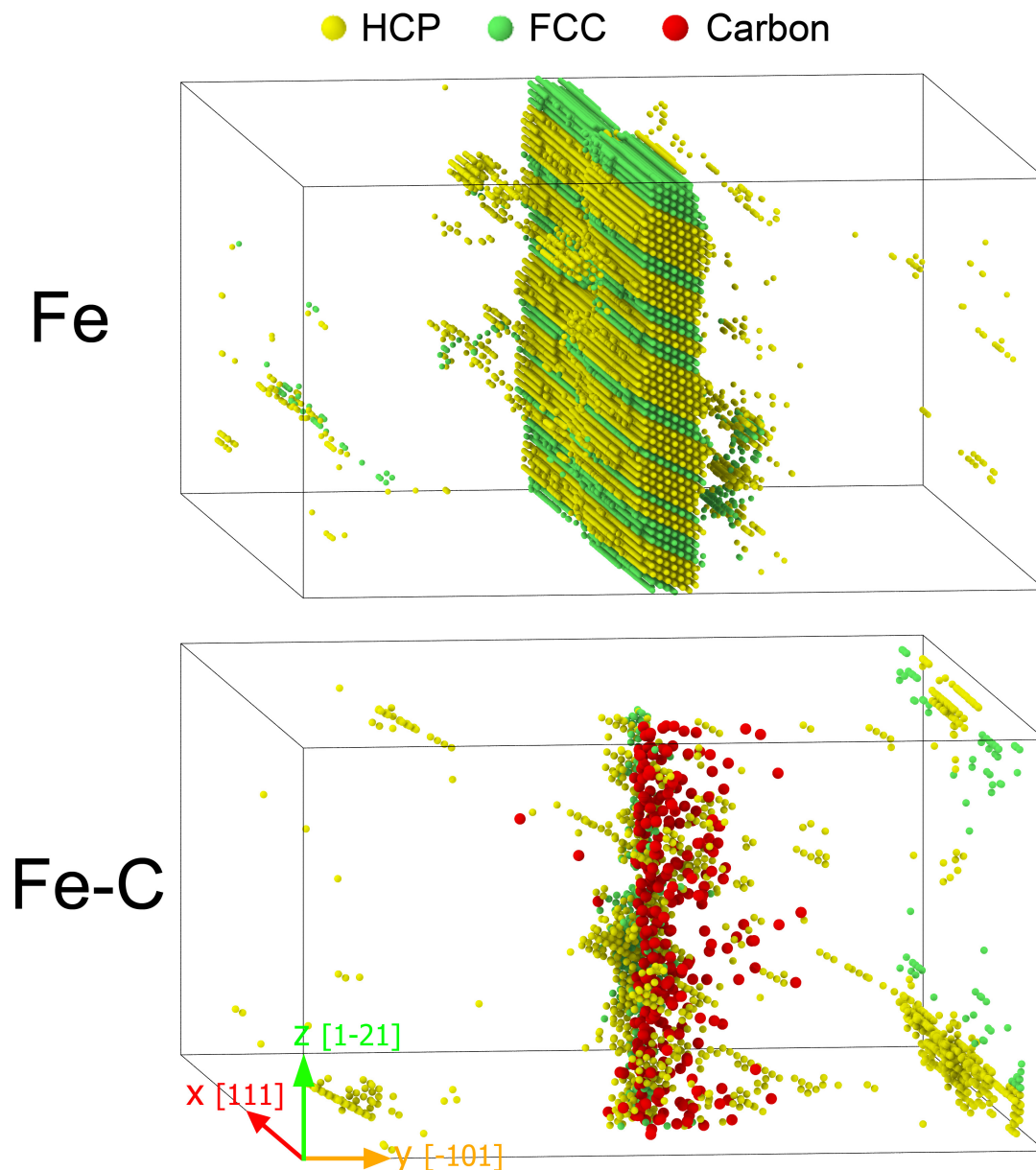
Figure 12. Snapshots of the dense phase at 6% strain of the sample containing an edge dislocation and a Cottrell atmosphere are shown on top and bottom, respectively. Atoms are colored by their local structure or atom type (red, carbon; yellow, hcp; green, fcc).

3.5. Comparison

In summary, the hcp and fcc phase fraction versus strain for all configurations are shown in Figure 13. We found that, for larger twin areas, the strain required to complete the transition process is reduced. The transformation process initiates first for crystals containing twin boundaries. Compared to the propagation of hcp clusters in perfect pure iron single-crystals under hydrostatic compression, the appearance of an edge dislocation on the ($\bar{1}01$) plane delayed the propagation process of the hcp phase although the nucleation of hcp takes place at both kinks of the buckling dislocations. The nucleation of a few hcp clusters starts inside the Cottrell atmosphere, but the carbon cloud highly limits the growth of these clusters. Figure 13 shows that the hcp phase fraction of single-crystals

containing twins is highest compared to the other simulations in this works. The fraction is by 10% higher than for the defect-free single-crystal. For the crystal containing an edge dislocation, nearly the same amount of metastable hcp phase and fcc has been recorded (45%). A reason could be that the existence of line dislocations under hydrostatic compression is related to twins in the parent material before the bcc/hcp phase transformation. The appearance of twins results in a large fraction of fcc after the transformation. In contrast, the development of the hcp phase starts in the bulk, and dominates the development of closed-packed phases during the transition. The phase fraction of this sample is almost 60% of hcp, 25% of fcc and we find only a negligible amount of atoms belonging to the dislocation or other defects at the end of the simulation.
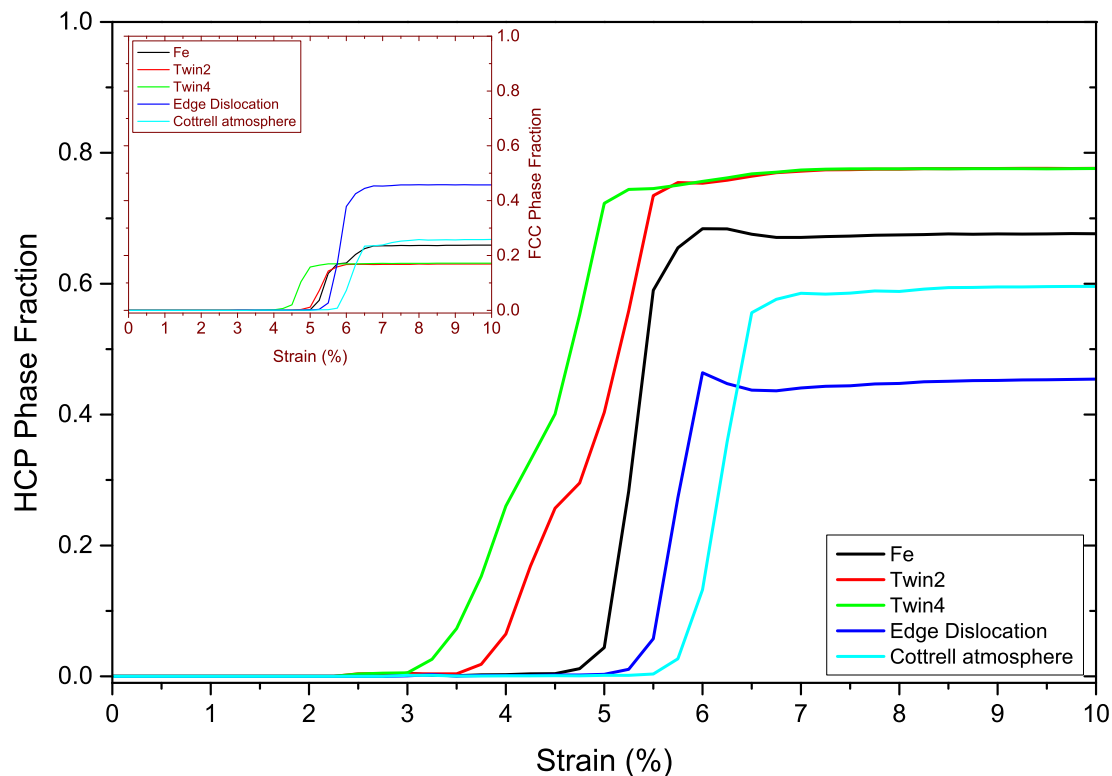

Figure 13. Hexagonal close-packed phase fraction versus strain for simulations of the sample with two twin surfaces (red), four twin surfaces (green), edge dislocations (blue) and Cottrell atmosphere (cyan) and pure iron single-crystals (black). Fcc fractions for all five simulations are embedded in the top left figure.

Note that the pressure induced phase transformation also strongly depends on the strain rate [67]. At low strain rates, the growth of the new phase is driven by thermal activation. At higher strain rates, the dislocation mobility is limited through energy dissipation of phonon modes. This is the reason the transition is delayed for high strain rates [68].

4. Conclusions

We determined the effects of three common types of defects to the pressure-induced transformation in iron. This study showed that, under hydrostatic compression the orientation, relation $\{110\}_{bcc} \parallel \{0001\}_{hcp}$ is preferred. Defects as edge dislocation and twin boundaries ease the nucleation of the hcp phase. The nucleation behavior is different to the results for pure iron single-crystals where the hcp clusters are formed randomly inside the bulk and differ in size and orientation [18,69]. The hcp phase forms at the cohesive twin boundaries as dense clusters. At higher strain, dense clusters are found in the bulk material. Interfaces between these clusters are twin boundaries of the daughter

phase because the orientations of the clusters of the new phase are different. Larger twin areas in bcc require smaller negative volume change to proceed to the transition process.

To test the ability of the interatomic potential to capture the mobility of edge dislocations, we examined two Frank–Read sources under shear loading and compared the result to DDD simulations. The mobilities of $1/2[111]\,(01\bar{1})$ edge dislocations, and $1/2[111]\,(\bar{1}2\bar{1})$ under shear loadings show different behavior, in agreement with available results from the literature. Surprisingly, unlike for fcc crystals showing dislocation multiplication from Frank–Read sources, for bcc, energetically-costly edge segments are generated, and no screw arms appear in the DDD simulations. This requires much greater stress, and, therefore, we did not observe the multiplication of dislocations.

For the crystals containing an edge dislocation $1/2[111]\,(\bar{1}01)$, under hydrostatic compression, the process begins with buckling of the cell structure in the dislocations. A large amount of fcc was found, attributed to the relation between the instability of the edge dislocation and twinning in the parent material before the transformation takes place.

The investigation of the Cottrell atmosphere shows that dense clusters first nucleate inside the atmosphere but cannot propagate; the transformation of the single-crystal starts from hcp clusters in the bulk material. Hardening effects due to the Cottrell atmosphere are observed, as a consequence of delaying the propagation of the dense phase.

Future investigations will cover atomistic mechanisms of dislocation unpinning from Cottrell atmospheres. The influence of more realistic dislocation networks as originating from nanoindentation tests will be evaluated. The influence of carbon segregation at grain boundaries will also be studied to evaluate the impact of carbon on material strength.

References

1. Bancroft, D.; Peterson, E.L.; Minshall, S. Polymorphism of Iron at High Pressure. *J. Appl. Phys.* **1956**, *27*, 291–298. [CrossRef]

2. Jamieson, J.C.; Lawson, A.W. X-ray Diffraction Studies in the 100 Kilobar Pressure Range. *J. Appl. Phys.* **1962**, *33*, 776–780. [CrossRef]

3. Bassett, W.A.; Huang, E. Mechanism of the Body-Centered Cubic–Hexagonal Close-Packed Phase Transition in Iron. *Science* **1987**, *238*, 780–783. [CrossRef] [PubMed]

4. Dewaele, A.; Denoual, C.; Anzellini, S.; Occelli, F.; Mezouar, M.; Cordier, P.; Merkel, S.; Véron, M.; Rausch, E. Mechanism of the α-ϵ phase transformation in iron. *Phys. Rev. B* **2015**, *91*, 174105. [CrossRef]

5. Kadau, K. Microscopic View of Structural Phase Transitions Induced by Shock Waves. *Science* **2002**, *296*, 1681–1684. [CrossRef] [PubMed]

6. Kalantar, D.H.; Belak, J.F.; Collins, G.W.; Colvin, J.D.; Davies, H.M.; Eggert, J.H.; Germann, T.C.; Hawreliak, J.; Holian, B.L.; Kadau, K.; et al. Direct Observation of the α-ϵ Transition in Shock-Compressed Iron via Nanosecond X-ray Diffraction. *Phys. Rev. Lett.* **2005**, *95*, 075502. [CrossRef] [PubMed]

7. Boehler, R.; Santamaría-Pérez, D.; Errandonea, D.; Mezouar, M. Melting, density, and anisotropy of iron at core conditions: New x-ray measurements to 150 GPa. *J. Phys. Conf. Ser.* **2008**, *121*, 022018. [CrossRef]

8. Sinmyo, R.; Hirose, K.; Ohishi, Y. Melting curve of iron to 290 GPa determined in a resistance-heated diamond-anvil cell. *Earth Planet. Sci. Lett.* **2019**, *510*, 45 – 52. [CrossRef]

9. Gunkelmann, N.; Tramontina, D.R.; Bringa, E.M.; Urbassek, H.M. Morphological changes in polycrystalline Fe after compression and release. *J. Appl. Phys.* **2015**, *117*, 085901. [CrossRef]

10. Ekman, M.; Sadigh, B.; Einarsdotter, K.; Blaha, P. Ab initio study of the martensitic bcc-hcp transformation in iron. *Phys. Rev. B* **1998**, *58*, 5296–5304. [CrossRef]

11. Herper, H.C.; Hoffmann, E.; Entel, P. Ab initio full-potential study of the structural and magnetic phase stability of iron. *Phys. Rev. B* **1999**, *60*, 3839–3848. [CrossRef]

12. Friák, M.; Šob, M. Ab initio study of the bcc-hcp transformation in iron. *Phys. Rev. B* **2008**, *77*, 174117. [CrossRef]

13. Jafari, M.; Nobakhti, M.; Jamnezhad, H.; Bayati, K. Density functional theory study of the $\alpha \rightarrow \omega$ martensitic transformation in titanium induced by hydrostatic pressure. *Condens. Matter Phys.* **2013**, *16*, 33703. [CrossRef]

14. Errandonea, D.; Meng, Y.; Somayazulu, M.; Häusermann, D. Pressure-induced $\alpha \rightarrow \omega$ transition in titanium metal: A systematic study of the effects of uniaxial stress. *Phys. B Condens. Matter* **2005**, *355*, 116–125. [CrossRef]

15. Trinkle, D.R.; Hennig, R.G.; Srinivasan, S.G.; Hatch, D.M.; Jones, M.D.; Stokes, H.T.; Albers, R.C.; Wilkins, J.W. New Mechanism for the α to ω Martensitic Transformation in Pure Titanium. *Phys. Rev. Lett.* **2003**, *91*, 025701. [CrossRef]

16. Friák, M.; Hickel, T.; Körmann, F.; Udyansky, A.; Dick, A.; von Pezold, J.; Ma, D.; Kim, O.; Counts, W.; Šob, M.; et al. Determining the Elasticity of Materials Employing Quantum-mechanical Approaches: From the Electronic Ground State to the Limits of Materials Stability. *Steel Res. Int.* **2011**, *82*, 86–100. [CrossRef]

17. Fisher, J. Application of nucleation theory to isothermal martensite. *Acta Metall.* **1953**, *1*, 32–35. [CrossRef]

18. Luu, H.T.; Gunkelmann, N. Pressure-induced phase transformations in Fe-C: Molecular dynamics approach. *Comput. Mater. Sci.* **2019**, *162*, 295–303. [CrossRef]

19. Harrison, R.J.; Voter, A.F.; Chen, S.P. *Atomistic Simulation of Materials: Beyond Pair Potentials*; Number 1; A Division of Plenum Publishing Corporation: New York, NY, USA, 1994; pp. 281–286. [CrossRef]

20. Gunkelmann, N.; Bringa, E.M.; Kang, K.; Ackland, G.J.; Ruestes, C.J.; Urbassek, H.M. Polycrystalline iron under compression: Plasticity and phase transitions. *Phys. Rev. B* **2012**, *86*, 144111. [CrossRef]

21. Kadau, K.; Germann, T.C.; Lomdahl, P.S.; Holian, B.L. Atomistic simulations of shock-induced transformations and their orientation dependence in bcc Fe single crystals. *Phys. Rev. B* **2005**, *72*, 064120. [CrossRef]

22. Kadau, K.; Germann, T.C.; Lomdahl, P.S.; Albers, R.C.; Wark, J.S.; Higginbotham, A.; Holian, B.L. Shock Waves in Polycrystalline Iron. *Phys. Rev. Lett.* **2007**, *98*, 135701. [CrossRef] [PubMed]

23. Venables, J.A. The martensite transformation in stainless steel. *Philos. Mag. J. Sci.* **1962**, *7*, 35–44. [CrossRef]

24. Yang, X.S.; Sun, S.; Wu, X.L.; Ma, E.; Zhang, T.Y. Dissecting the Mechanism of Martensitic Transformation via Atomic-Scale Observations. *Sci. Rep.* **2014**, *4*, 6141. [CrossRef] [PubMed]

25. Veiga, R.G.A.; Perez, M.; Becquart, C.S.; Domain, C. Atomistic modeling of carbon Cottrell atmospheres in bcc iron. *J. Phys. Condens. Matter* **2012**, *25*, 025401. [CrossRef]

26. Veiga, R.; Goldenstein, H.; Perez, M.; Becquart, C. Monte Carlo and molecular dynamics simulations of screw dislocation locking by Cottrell atmospheres in low carbon Fe–C alloys. *Scr. Mater.* **2015**, *108*, 19–22. [CrossRef]

27. Queyreau, S.; Marian, J.; Gilbert, M.R.; Wirth, B.D. Edge dislocation mobilities in bcc Fe obtained by molecular dynamics. *Phys. Rev. B* **2011**, *84*, 064106. [CrossRef]

28. Daw, M.S.; Foiles, S.M.; Baskes, M.I. The embedded-atom method: A review of theory and applications. *Mater. Sci. Rep.* **1993**, *9*, 251–310. [CrossRef]

29. Gunkelmann, N.; Bringa, E.M.; Tramontina, D.R.; Ruestes, C.J.; Suggit, M.J.; Higginbotham, A.; Wark, J.S.; Urbassek, H.M. Shock waves in polycrystalline iron: Plasticity and phase transitions. *Phys. Rev. B* **2014**, *89*, 140102. [CrossRef]

30. Gunkelmann, N.; Bringa, E.M.; Urbassek, H.M. Influence of phase transition on shock-induced spallation in nanocrystalline iron. *J. Appl. Phys.* **2015**, *118*, 185902. [CrossRef]

31. Amadou, N.; de Resseguier, T.; Dragon, A.; Brambrink, E. Coupling between plasticity and phase transition in shock- and ramp-compressed single-crystal iron. *Phys. Rev. B* **2018**, *98*, 024104. [CrossRef]

32. Hepburn, D.J.; Ackland, G.J. Metallic-covalent interatomic potential for carbon in iron. *Phys. Rev. B* **2008**, *78*, 165115. [CrossRef]

33. Tschopp, M.A.; Solanki, K.N.; Gao, F.; Sun, X.; Khaleel, M.A.; Horstemeyer, M.F. Probing grain boundary sink strength at the nanoscale: Energetics and length scales of vacancy and interstitial absorption by grain boundaries in α-Fe. *Phys. Rev. B* **2012**, *85*, 064108. [CrossRef]

34. Hirel, P. Atomsk: A tool for manipulating and converting atomic data files. *Comput. Phys. Commun.* **2015**, *197*, 212–219. [CrossRef]

35. Osetsky, Y.N.; Bacon, D.J. An atomic-level model for studying the dynamics of edge dislocations in metals. *Model. Simul. Mater. Sci. Eng.* **2003**, *11*, 427–446. [CrossRef]

36. Bacon, D.; Osetsky, Y.; Rodney, D. Dislocation–Obstacle Interactions at the Atomic Level. In *Dislocations in Solids*; Elsevier: Amsterdam, The Netherlands, 2009; Chapter 88, pp. 1–90. [CrossRef]

37. Plimpton, S. Fast parallel algorithms for short-range molecular dynamics. *J. Comput. Phys.* **1995**, *117*, 1–19. [CrossRef]

38. Vo, N.Q.; Averback, R.S.; Bellon, P.; Caro, A. Limits of hardness at the nanoscale: Molecular dynamics simulations. *Phys. Rev. B* **2008**, *78*, 241402. [CrossRef]

39. Waseda, O.; Veiga, R.G.A.; Morthomas, J.; Chantrenne, P.; Becquart, C.S.; Ribeiro, F.; Jelea, A.; Goldenstein, H.; Perez, M. Formation of carbon Cottrell atmospheres and their effect on the stress field around an edge dislocation. *Scr. Mat.* **2016**, *129*, 16–19. [CrossRef]

40. Steinhardt, P.J.; Nelson, D.R.; Ronchetti, M. Bond-orientational order in liquids and glasses. *Phys. Rev. B* **1983**, *28*, 784–805. [CrossRef]

41. Honeycutt, J.D.; Andersen, H.C. Molecular dynamics study of melting and freezing of small Lennard-Jones clusters. *J. Phys. Chem.* **1987**, *91*, 4950–4963. [CrossRef]

42. Kelchner, C.L.; Plimpton, S.J.; Hamilton, J.C. Dislocation nucleation and defect structure during surface indentation. *Phys. Rev. B* **1998**, *58*, 11085–11088. [CrossRef]

43. Ackland, G.J.; Jones, A.P. Applications of local crystal structure measures in experiment and simulation. *Phys. Rev. B* **2006**, *73*, 054104. [CrossRef]

44. Stukowski, A. Structure identification methods for atomistic simulations of crystalline materials. *Model. Simul. Mater. Sci. Eng.* **2012**, *20*, 045021. [CrossRef]

45. Stukowski, A. Visualization and analysis of atomistic simulation data with OVITO–the Open Visualization Tool. *Model. Simul. Mater. Sci. Eng.* **2009**, *18*, 015012. [CrossRef]

46. de Koning, M.; Cai, W.; Bulatov, V.V. Anomalous Dislocation Multiplication in FCC Metals. *Phys. Rev. Lett.* **2003**, *91*, 025503. [CrossRef]

47. Shimokawa, T.; Kitada, S. Dislocation Multiplication from the Frank-Read Source in Atomic Models. *Mater. Trans.* **2014**, *55*, 58–63. [CrossRef]

48. Li, X.Y.; Yang, W. Atomistic simulations for the evolution of a U-shaped dislocation in fcc Al. *Phys. Rev. B* **2006**, *74*, 144108. [CrossRef]

49. Tsuru, T.; Aoyagi, Y.; Kaji, Y.; Shimokawa, T. Influence of Competition between Intragranular Dislocation Nucleation and Intergranular Slip Transfer on Mechanical Properties of Ultrafine-Grained Metals. *Mater. Trans.* **2013**, *54*, 1580–1586. [CrossRef]

50. Fitzgerald, S.P.; Aubry, S.; Dudarev, S.L.; Cai, W. Dislocation dynamics simulation of Frank-Read sources in anisotropic α-Fe. *Model. Simul. Mater. Sci. Eng.* **2012**, *20*, 045022. [CrossRef]

51. Po, G.; Cui, Y.; Rivera, D.; Cereceda, D.; Swinburne, T.D.; Marian, J.; Ghoniem, N. A phenomenological dislocation mobility law for bcc metals. *Acta Mater.* **2016**, *119*, 123–135. [CrossRef]

52. Po, G.; Ghoniem, N. A variational formulation of constrained dislocation dynamics coupled with heat and vacancy diffusion. *J. Mech. Phys. Solids* **2014**, *66*, 103–116. [CrossRef]

53. Domain, C.; Monnet, G. Simulation of Screw Dislocation Motion in Iron by Molecular Dynamics Simulations. *Phys. Rev. Lett.* **2005**, *95*, 215506. [CrossRef]

54. Vitek, V.; Smith, D.A.; Pond, R.C. Structure of tilt grain boundaries in b.c.c. metals. *Philos. Mag. A* **1980**, *41*, 649–663. [CrossRef]

55. Hahn, E.N.; Fensin, S.J.; Germann, T.C.; Meyers, M.A. Symmetric tilt boundaries in body-centered cubic tantalum. *Scr. Mater.* **2016**, *116*, 108–111. [CrossRef]

56. Forbes, J.W. *Shock Wave Compression of Condensed Matter*; Springer: Berlin/Heidelberg, Germany, 2012. [CrossRef]

57. Burgers, W. On the process of transition of the cubic-body-centered modification into the hexagonal-close-packed modification of zirconium. *Physica* **1934**, *1*, 561–586. [CrossRef]

58. Wang, F.M.; Ingalls, R. Iron bcc-hcp transition: Local structure from x-ray-absorption fine structure. *Phys. Rev. B* **1998**, *57*, 5647–5654. [CrossRef]

59. Meyers, M.; Jarmakani, H.; Bringa, E.; Remington, B. Chapter 89 Dislocations in Shock Compression and Release. In *Dislocations in Solids*; Elsevier: Amsterdam, The Netherlands, 2009; pp. 91–197. [CrossRef]

60. Turneaure, S.J.; Renganathan, P.; Winey, J.; Gupta, Y. Twinning and Dislocation Evolution during Shock Compression and Release of Single Crystals: Real-Time X-ray Diffraction. *Phys. Rev. Lett.* **2018**, *120*, 265503. [CrossRef]

61. Meyers, M.A.; Murr, L.E. (Eds.) *Shock Waves and High-Strain-Rate Phenomena in Metals*; Springer US: New York, NY, USA, 1981. [CrossRef]

62. Vítek, V. Dissociation of Dislocations on {110} Planes in Anisotropie B.C.C. Metals. *Phys. Status Solidi B* **1966**, *15*, 557–566. [CrossRef]

63. Kuznetsov, A.; Gornostyrev, Y.; Katsnelson, M.; Trefilov, A. Effect of the dislocations on the kinetics of a martensitic transition. *Mater. Sci. Eng. A* **2001**, *309–310*, 168–172. [CrossRef]

64. Cohen, J.; Hinton, R.; Lay, K.; Sass, S. Partial dislocations on the {110} planes in the b.c.c. lattice. *Acta Metall.* **1962**, *10*, 894–895. [CrossRef]

65. Clouet, E.; Garruchet, S.; Nguyen, H.; Perez, M.; Becquart, C.S. Dislocation interaction with C in α-Fe: A comparison between atomic simulations and elasticity theory. *Acta Mater.* **2008**, *56*, 3450–3460. [CrossRef]

66. Wilde, J.; Cerezo, A.; Smith, G.D.W. Three-dimensional atomic-scale mapping of a Cottrell atmosphere around a dislocation in iron. *Scr. Mater.* **2000**, *43*, 39–48. [CrossRef]

67. Grujicic, M.; Olson, G.B. Dynamics of Martensitic Interfaces. *Interface Sci.* **1998**, *6*, 155–164. [CrossRef]

68. Smith, R.F.; Eggert, J.H.; Swift, D.C.; Wang, J.; Duffy, T.S.; Braun, D.G.; Rudd, R.E.; Reisman, D.B.; Davis, J.P.; Knudson, M.D.; et al. Time-dependence of the alpha to epsilon phase transformation in iron. *J. Appl. Phys.* **2013**, *114*, 223507. [CrossRef]

69. Shao, J.L.; Wang, P.; Zhang, F.G.; He, A.M. Hcp/fcc nucleation in bcc iron under different anisotropic compressions at high strain rate: Molecular dynamics study. *Sci. Rep.* **2018**, *8*, 7650. [CrossRef] [PubMed]